nature portfolio
https://doi.org/10.1038/s41586-026-10696-0

Supplementary information

GW250114 reveals signatures of post-merger black-hole horizon

In the format provided by the authors and unedited

GW250114 reveals signatures of post-merger black hole horizon
Supplementary Information

Neil Lu, Sizheng Ma, Ornella J. Piccinni, Yanbei Chen, and Ling Sun

I. NEAR-HORIZON WAVE EMISSION AND HORIZON MODES

Direct waves and horizon modes are outgoing waves emitted near a black hole's horizon. The appearance of this emission, however, depends on the observer's frame. Below, we take a pedagogical approach to illustrate how different observers perceive this process.

To formulate this more precisely, we introduce four coordinate systems (see Supplementary Table 1), each corresponding to a family of observers whose spatial locations are arranged in a specific manner. Every observer carries a clock, and these clocks are synchronized and tick according to the time coordinate of their respective system. We describe the same process in alternative coordinate systems, each offering a distinct observational perspective. The Boyer–Lindquist coordinates (t, r, θ, ϕ) provide perhaps the most familiar description, as they align closely with our intuitive notions of spacetime decomposition and serve as the natural coordinate system for distant observers. Supplementary Fig. 1 (a) shows a particle falling down a black hole, viewed by Boyer–Lindquist observers. The particle asymptotically approaches the horizon at r_+ and appears to freeze there, never actually crossing it. Rays emitted closer to the horizon take progressively longer to reach a finite distance away from the black hole; as a result, they are increasingly stretched (redshifted) at late times. Meanwhile, the left panel of Supplementary Fig. 2 shows the corresponding azimuthal motion: rays emitted near the horizon swirl more angles before propagating outward.

The radial motion is described more naturally using the tortoise radial coordinate r_*:

$$r_* = \int \frac{r^2 + \chi^2}{\Delta} dr, \tag{S1}$$

with $\Delta = r^2 - 2r + \chi^2$. This coordinate maps the near-horizon region to an unbounded domain ($r = r_+$ is mapped to $r_* = -\infty$), which naturally encodes the near-horizon gravitational redshift effect and thus provides a more suitable way to describe the propagation of outgoing rays. Indeed, as illustrated in Supplementary Fig. 1 (b), rays that are equally spaced in r_* remain equally spaced as they propagate outward. These rays, on the other hand, are emitted at exponentially decreasing intervals with respect to the emitter's proper time. Specifically, the emitter's motion near the horizon satisfies, see, i.e., Eq. (2.4) in [1]

$$\frac{dr}{d\tau} \propto \text{const}, \tag{S2}$$

which implies that the emitter's proper time τ is proportional to $r \sim r_+ + e^{2\kappa r_*}$. Consequently, a sequence of rays that are equally spaced in r_* (and thus received at equal time intervals by a distant observer) are emitted at exponentially shrinking proper-time intervals $\Delta\tau$ by the infalling source.

The ingoing Eddington–Frankestein coordinate system $(t_{\text{in}}, r, \theta, \phi_{\text{in}})$ is defined as:

$$t_{\text{in}} = t + r_* - r, \tag{S3a}$$

$$\phi_{\text{in}} = \phi + \int \frac{\chi}{\Delta} dr, \tag{S3b}$$

	Coordinates	Horizon	Particle	Observer	Outgoing rays	Features
(a)	Boyer–Lindquist (t, r)	future/past horizons both at $r = r_+$	asymptote to r_+ in the future	constant position	asymptote to r_+ in the past, 45° in the future	particle and rays freeze on the horizon
(b)	Tortoise (t, r_*)	outside range	nearly 45°	constant position	45°	near-horizon motions simplified
(c)	Ingoing EF (t_{in}, r)	future/past horizons both at $r = r_+$	penetrates horizon	constant position	asymptote to r_+ in the past, 45° in the future	regular near the future horizon
(d)	Kruskal (U, V)	All resolved at $UV = 0$	penetrates horizon	hyperbolic worldline	45°	regular at all horizons

Table S1: Comparison between coordinate systems.

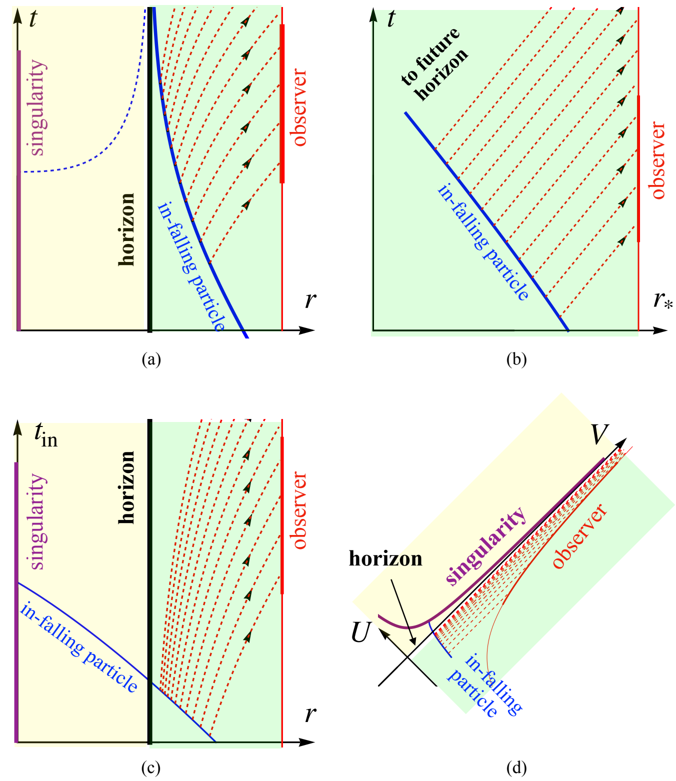

Figure S1: Four coordinate systems depicting the same particle falling into a black hole and crossing the horizon in finite proper time. The particle emits rays at exponentially decreasing proper-time intervals before horizon crossing. (a) In Boyer–Lindquist coordinates, the particle asymptotes to the horizon without reaching it, and the emitted rays appear to be spread out over all times. (b) In the tortoise coordinate system, which is well adapted for illustrating wave propagation, the horizon is at $r_* \to -\infty$; the ingoing trajectory of the particle approaches 45° with $dr_*/dt = -1$. The emitted outgoing rays satisfy $dr_*/dt = 1$. (c) In ingoing Eddington–Finkelstein coordinates, the particle smoothly crosses the horizon, and the shrinking proper-time intervals between ray emissions before horizon-crossing are evident. (d) In Kruskal coordinates that maximally extend a Kerr spacetime, the particle follows an approximately constant-V trajectory, while the outgoing rays follow constant-U lines.

where the coordinate time $t_{\rm in}$ corresponds to the clocks carried by observers whose ticking rate depends on the radial position. In this coordinate system, ingoing principal null geodesics trace straight coordinate lines,

$$t_{\rm in} + r = \text{const}, \tag{S4}$$

with no azimuthal motion, i.e., $\phi_{\rm in} = \text{const}$. The ingoing Eddington–Finkelstein coordinates are therefore well suited for describing trajectories that fall into the black hole, such as the plunging motion relevant to binary coalescences. An example of such a trajectory is shown by the blue curve in Supplementary Fig. 1 (c), which reaches the horizon at a finite coordinate time $t_{\rm in}$ and smoothly crosses it. Outgoing rays emitted along the way (red dashed curves) satisfy

$$\frac{dt_{\rm in}}{dr} = 2\frac{r^2 + a^2}{\Delta} - 1, \tag{S5}$$

indicating that the closer the emission occurs to the horizon, the longer it takes for the rays to escape to distant observers. Similarly, the angular evolution of outgoing rays is given by

$$\frac{d\phi_{\rm in}}{dt_{\rm in}} = \frac{2\chi}{2(r^2 + \chi^2) - \Delta}. \tag{S6}$$

The right panel of Supplementary Fig. 2 illustrates the azimuthal motion: rays that take longer to propagate outward undergo more angular winding around the black hole.

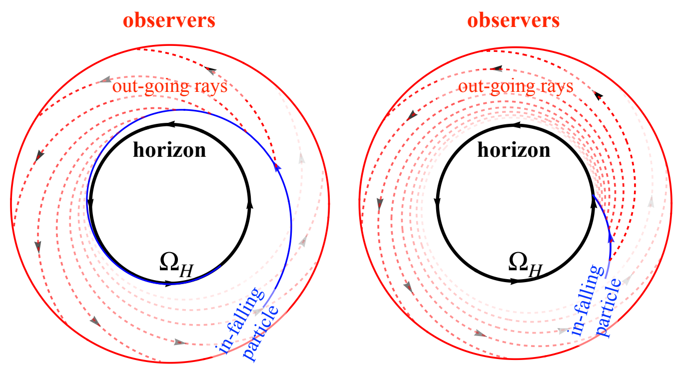

Figure S2: Frame-dragging in the near-horizon region of a Kerr black hole, whose horizon rotates at an angular frequency Ω_H relative to distant observers. The left and right panels show top views of the coordinate systems in Supplementary Fig. 1 (a) and (c), respectively, plotted using the azimuthal angle measured by distant observers.

Finally, the Kruskal coordinate system $(U, V, \theta, \tilde{\phi})$ is defined as [2]

$$U = -e^{-\kappa(t-r_*)}, \tag{S7a}$$
$$V = e^{\kappa(t+r_*)}, \tag{S7b}$$
$$\tilde{\phi} = \phi - \Omega_H t. \tag{S7c}$$

As illustrated in Supplementary Fig. 1 (d), Kruskal observers correspond to the ingoing principal null geodesics ($V = \text{const}$) that fall into the black hole horizon and the outgoing principal null geodesics ($U = \text{const}$) that emerge from the white hole horizon. This Kruskal system remains regular across the horizons and provides a well-behaved description of the maximal extension of the Kerr spacetime around the bifurcation sphere ($U = V = 0$). The blue curve in Supplementary Fig. 1 (d) represents a plunging trajectory. As the particle accelerates to nearly the speed of light near the horizon, its path becomes approximately aligned with a constant-V line and crosses the horizon ($U = 0$) smoothly. The emitted outgoing rays form straight coordinate lines $U = \text{const}$ (red dashed lines). A distant observer, located at a fixed radius r, follows a worldline satisfying $UV = \text{const}$ (red solid curve). The time intervals between the received signals are stretched (redshifted) at late times.

The outgoing waves emitted by the plunging particle can be represented by an analytic function ψ of the retarded time U and $\tilde{\phi}$, whose Taylor expansion reads

$$\psi(U, \tilde{\phi}) \sim \sum_{n,m} c_{n,m} U^n e^{im\tilde{\phi}}, \tag{S8}$$

where n and m are integers, and $c_{n,m}$ are coefficients. The corresponding signals received by the distant observer follow the same functional dependence and can be interpreted as a superposition of an infinite set of horizon modes

$$U^n e^{im\tilde{\phi}} \sim e^{-i\omega_H^{(mn)} t} e^{im\phi}, \tag{S9}$$

with

$$\omega_H^{(mn)} = m\Omega_H - in\kappa. \tag{S10}$$

Here we have used Eqs. (S7a) and (S7c).

Another feature of horizon modes emerges from the near-horizon geometry. Using the Rindler coordinates

$$dt^2 = -\kappa^2 \rho^2 dt^2 + d\rho^2 + \gamma_{AB} dX^A dX^B\,, \tag{S11}$$

with $\rho \approx \sqrt{2(r - r_+)/\kappa} \propto e^{\kappa r_*}$, the metric can be Euclideanized via a Wick rotation $t = i\tau$. Identifying $\tau \to \tau + 2\pi\kappa$ makes a locally smooth space free from conical singularity [3]. Horizon modes are single-valued smooth functions in this Euclidean space, while other modes are multi-valued.

II. SCREENING OF THE HORIZON MODES

In Sec. I, we show that the horizon modes, $\omega_H^{(mn)}$ defined in Eq. (S10), represent outgoing waves emitted near the horizon. However, here we argue that these modes are entirely screened by the black hole potential barrier and do not contribute to the direct waves observed at infinity.

The most direct argument follows Refs. [4, 5], which explicitly show that the black hole's greybody factor, the transmissivity of outgoing waves emitted from the past horizon toward future null infinity, vanishes exactly at $\omega_H^{(mn)}$. This property has also been discussed in the context of the Kerr/CFT correspondence [6, 7] and in classical literature on black hole perturbation theory. For example, the energy absorption coefficient Γ in Eq. (4.7) of Ref. [8] vanishes at poles of $A_{\rm in}^{s\nu} A_{\rm in}^{-s\nu}$, which, according to their Eq. (4.2), includes $m\Omega_H - i(1+n\pm s)\kappa$ with s the spin weight of the field and $n = 0, 1, 2, \ldots$.

Another instructive way to understand the screening effect is by considering the Hawking flux $\mathcal{N}_{\ell m}(\omega)$ at infinity for the (ℓ, m) mode:

$$\mathcal{N}_{\ell m}(\omega) = \frac{\Gamma_{\ell m}(\omega)}{\exp[\beta(\omega - m\Omega_H)] - 1}\,, \tag{S12}$$

where $\Gamma_{\ell m}(\omega)$ is the corresponding energy greybody factor, and $\beta = 2\pi/\kappa$ is the inverse temperature of the black hole. The Bose–Einstein factor in the denominator has poles precisely at the horizon mode frequencies $\omega_H^{(mn)}$. In this sense, the horizon modes can be interpreted as the Matsubara frequencies of the black hole [9], corresponding to those with negative imaginary parts. The vanishing of $\Gamma_{\ell m}(\omega)$ at $\omega_H^{(mn)}$ makes the flux $\mathcal{N}_{\ell m}(\omega)$ remain finite by canceling the divergences at these poles.

III. DIRECT WAVES

Although the horizon modes $\omega_H^{(mn)}$ are completely screened by the black hole potential barrier [4, 5], direct waves emitted not too close to the horizon can still reach distant observers, as noted in Ref. [4]. In the following, we briefly summarize the derivation of the analytic waveform for the direct waves used in the main text, and refer the reader to [4] for further details.

The gravitational-wave strain can be obtained by two time integrations of the Weyl scalar Ψ_4. Using the Teukolsky equation [10, 11], the asymptotic form of Ψ_4 observed at infinity can be written as

$$[r\Psi_4(u)]_{r\to\infty,\ell m} = \int d\omega e^{-i\omega u} Z_{\ell m\omega}, \tag{S13}$$

where u is the retarded time, and Ψ_4 has been decomposed into spin-weighted spheroidal harmonics labeled by (ℓ, m). The quantity $Z_{\ell m\omega}$ denotes the Fourier mode at frequency ω, given by

$$Z_{\ell m\omega} = \frac{1}{2i\omega B^{\rm in}_{\ell m\omega}} \int dr \frac{R^{\rm in}_{\ell m\omega} S_{\ell m\omega}}{\Delta^2}, \tag{S14}$$

where $\Delta = (r - r_+)(r - r_-)$ and $r_\pm$ denote the radii of the event and Cauchy horizons, respectively. $S_{\ell m\omega}$ is the source term contributed by the perturber. $R^{\rm in}_{\ell m\omega}$ is the ingoing homogeneous solution to the Teukolsky equation, satisfying the boundary conditions

$$R^{\rm in}_{\ell m\omega}(r) = \begin{cases} \Delta^2 e^{-ikr_*} & r \to r_+ \\ B^{\rm out}_{\ell m\omega} r^3 e^{i\omega r_*} + r^{-1} B^{\rm in}_{\ell m\omega} e^{-i\omega r_*} & r \to \infty \end{cases}, \tag{S15}$$

with $k = \omega - m\Omega_H$.

Here we focus on the contribution from waves sourced in the near-horizon region. Specifically, we restrict the integration in Eq. (S14) to $r \sim r_+$, under which the expression simplifies to [1, 4, 12]

$$Z_{\ell m\omega} = \hat{D}_{\ell m\omega} \tilde{Z}_{\ell m\omega} \int dt e^{i\omega t - im\phi(t)} e^{-i(k+2i\kappa)r_*(t)}, \tag{S16}$$

where $\phi(t)$ and $r_*(t)$ denote the orbital phase and tortoise radial coordinate of the perturber, respectively. The explicit forms of $\hat{D}_{\ell m\omega}$ and $\tilde{Z}_{\ell m\omega}$ are lengthy and not particularly illuminating, and we refer the reader to [1, 4, 12] for their full expressions.

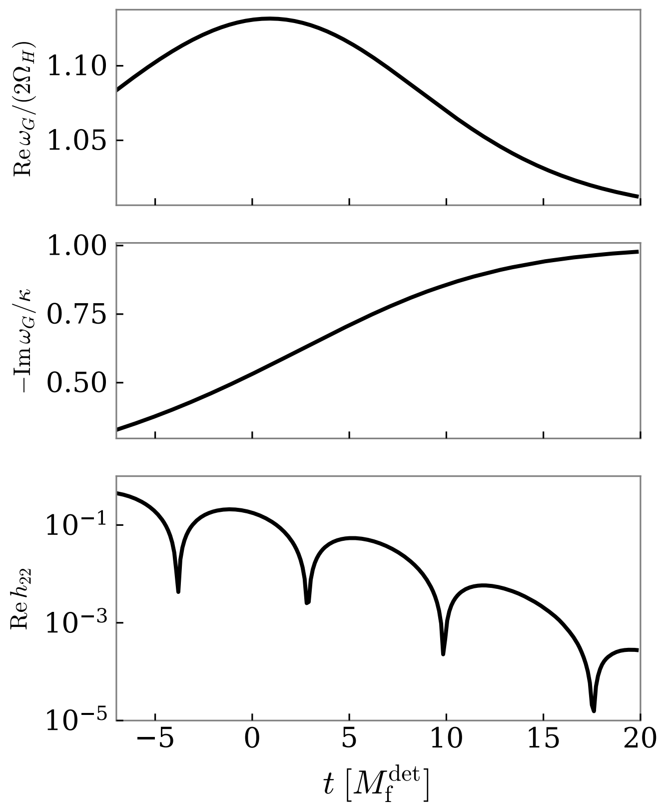

Figure S3: Time evolution of the real (top) and imaginary (middle) parts of $\omega_G(t)$, as defined in Eq. (S21). The resulting $\omega_G(t)$ is used to construct the direct-wave component of the GW250114-like numerical relativity waveform (bottom), corresponding to the red dashed curve in Fig. 3.

Plugging Eq. (S16) into (S13), we obtain

$$[r\Psi_4(u)]_{r\to\infty,\ell m} = \int d\omega \int dt \hat{D}_{\ell m\omega} \tilde{Z}_{\ell m\omega} e^{i\omega(t-u)-im\phi(t)} e^{-i(k+2i\kappa)r_*(t)}. \tag{S17}$$

The integrand has a saddle point in the $t-\omega$ plane, determined by

$$u = t - r_*(t), \tag{S18}$$

$$\omega = \omega_G(t), \tag{S19}$$

where the first condition reflects the direct propagation of the emitted wave. The instantaneous complex frequency $\omega_G(t)$ is given by [4]:

$$\omega_G(t) = 2\hat{\Omega}(t) - i\hat{\kappa}(t), \tag{S20}$$

where

$$\hat{\Omega}(t) = \frac{\beta\Omega_H + \dot{\phi}}{1+\beta}, \tag{S21a}$$

$$\hat{\kappa} = \frac{2\beta}{1+\beta}\kappa, \tag{S21b}$$

with $\beta = |dr_*/dt|$ denoting the radial velocity in the tortoise coordinate, and $\dot{\phi} = d\phi/dt$ the instantaneous angular velocity. Here we have chosen $m = 2$.

To obtain $\omega_G(t)$ for GW250114, we evolve the geodesic equations for a test particle plunging in the equatorial plane

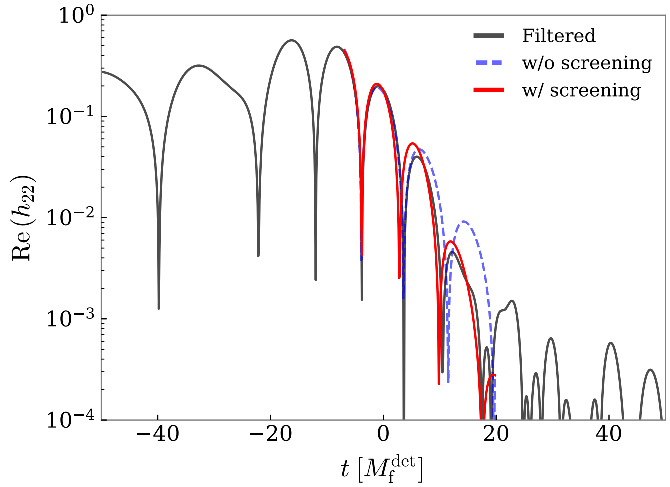

Figure S4: Comparison between the unscreened waveform model (blue dashed), $e^{-i\int \omega_G(t)dt}$, screened waveform defined in Eq. (5) (red solid), and the filtered quadrupolar harmonic ($\ell = m = 2$) of the NRSur7dq4 waveform (black).

of a Kerr black hole [2, 13]:

$$r^2 \frac{dt}{d\tau} = -\chi(\chi E - L_z) + \frac{r^2+\chi^2}{\Delta} P(r)\,, \tag{S22}$$

$$\frac{dr}{d\tau} = -\sqrt{\frac{2}{3r_I}}\left(\frac{r_I}{r} - 1\right)^{3/2}\,, \tag{S23}$$

$$r^2 \frac{d\phi}{d\tau} = -(\chi E - L_z) + \frac{\chi}{\Delta} P(r)\,, \tag{S24}$$

where $P(r) = E(r^2 + \chi^2) - \chi L_z$. We set $\chi = 0.672509$, the maximum-a-posteriori value inferred for the remnant black hole in GW250114 [14–16], and adopt the corresponding values of the energy E, angular momentum L_z, and radius r_I of the innermost stable circular orbit:

$$E = \frac{r_I^{3/2} - 2r_I^{1/2} + \chi}{r_I^{3/4}\sqrt{r_I^{3/2} - 3r_I^{1/2} + 2\chi}}, \tag{S25a}$$

$$L_z = \frac{r_I^2 - 2\chi r_I^{1/2} + \chi^2}{r_I^{3/4}\sqrt{r_I^{3/2} - 3r_I^{1/2} + 2\chi}}. \tag{S25b}$$

The particle is initially placed at $r = r_I - 10^{-5}$ and allowed to plunge into the black hole.

Supplementary Fig. 3 shows the time evolution of the real (top) and imaginary (middle) parts of $\omega_G(t)$ over the same time window considered in Fig. 3 ($t \in [-7, 20]M_\mathrm{f}^\mathrm{det}$), expressed in units of $2\Omega_H$ and κ, respectively. The real part of the frequency remains above $2\Omega_H$ throughout this interval, consistent with the free-frequency fits during the time interval shown in Fig. 4. In contrast, the imaginary part stays below κ, but grows as the particle continues to accelerate radially and β increases, again in agreement with the trend observed in Fig. 4.

In Supplementary Fig. 4, we investigate the screening effect from the potential barrier by comparing an unscreened waveform model (blue dashed), $e^{-i\int \omega_G(t)dt}$, with the screened waveform given by Eq. (5), as well as the filtered quadrupolar harmonic. The difference becomes more pronounced at late times ($t \gtrsim 5M_\mathrm{f}^\mathrm{det}$), when $\omega_G(t)$ evolves sufficiently close to ω_H. Within the analysis windows used in the main text, $[t_\mathrm{start}, t_\mathrm{start} + 0.2\,\mathrm{s}]$ with $t_\mathrm{start} \in [-7, -3]M_\mathrm{f}^\mathrm{det}$, the results are dominated by the first wave cycle. Supplementary Fig. 4 indicates that the screening effect plays a minor role in this early-time regime. Thus, the increasing damping rates observed in Fig. 4 are primarily driven by the evolution of $\hat{\kappa}(t)$ [Eq. (S21b)], as shown in the middle panel of Supplementary Fig. 3.

REFERENCES

[1] Y. Mino and J. Brink, Gravitational Radiation from Plunging Orbits: Perturbative Study, Phys. Rev. D **78**, 124015 (2008), arXiv:0809.2814 [gr-qc].

[2] B. O'Neill, *The geometry of Kerr black holes* (Courier Corporation, 2014).

[3] G. W. Gibbons and S. W. Hawking, Action integrals and partition functions in quantum gravity, Physical Review D **15**, 2752 (1977).

[4] N. Oshita, S. Ma, Y. Chen, and H. Yang, Probing Direct Waves in Black Hole Ringdowns, (2025), arXiv:2509.09165 [gr-qc].

[5] A. Zimmerman, Z. Mark, and Y. Chen, Revisiting the emission from an extreme mass ratio plunge (2018), presented the APS April Meeting, Columbus, OH, 2018.

[6] A. Castro, J. M. Lapan, A. Maloney, and M. J. Rodriguez, Black hole monodromy and conformal field theory, Physical Review D—Particles, Fields, Gravitation, and Cosmology **88**, 044003 (2013).

[7] I. Bredberg, T. Hartman, W. Song, and A. Strominger, Black hole superradiance from kerr/cft, Journal of High Energy Physics **2010**, 1 (2010).

[8] S. Mano, H. Suzuki, and E. Takasugi, Analytic solutions of the Teukolsky equation and their low frequency expansions, Prog. Theor. Phys. **95**, 1079 (1996), arXiv:gr-qc/9603020.

[9] T. Matsubara, A new approach to quantum-statistical mechanics, Progress of Theoretical Physics **14**, 351 (1955).

[10] S. A. Teukolsky, Perturbations of a rotating black hole. 1. Fundamental equations for gravitational electromagnetic and neutrino field perturbations, Astrophys. J. **185**, 635 (1973).

[11] S. A. Teukolsky, Rotating black holes: Separable wave equations for gravitational and electromagnetic perturbations, Phys. Rev. Lett. **29**, 1114 (1972).

[12] A. Zimmerman and Y. Chen, New Generic Ringdown Frequencies at the Birth of a Kerr Black Hole, Phys. Rev. D **84**, 084012 (2011), arXiv:1106.0782 [gr-qc].

[13] A. Mummery and S. Balbus, Inspirals from the Innermost Stable Circular Orbit of Kerr Black Holes: Exact Solutions and Universal Radial Flow, Phys. Rev. Lett. **129**, 161101 (2022), arXiv:2209.03579 [gr-qc].

[14] A. G. Abac, I. Abouelfettouh, F. Acernese, *et al.*, GW250114: Testing Hawking's Area Law and the Kerr Nature of Black Holes, Physical Review Letters **135**, 111403 (2025).

[15] A. G. Abac *et al.* (LIGO Scientific, Virgo, KAGRA), Black Hole Spectroscopy and Tests of General Relativity with GW250114, Phys. Rev. Lett. **136**, 041403 (2026).

[16] The LIGO Scientific Collaboration, the Virgo Collaboration, and the KAGRA Collaboration, GW250114_082203 data release, Gravitational Wave Open Science Center (2025), doi:10.7935/1g4j-2028.